International Communications in Heat and Mass Transfer 115 (2020) 104631

Contents lists available at ScienceDirect

International Communications in Heat and Mass Transfer

journal homepage: www.elsevier.com/locate/ichmt

Pore scale investigations on melting of phase change materials considering the interfacial thermal resistance

Wen-Zhen Fang[a,b,*], Yu-Qing Tang[a], Chun Yang[b], Wen-Quan Tao[a]

[a] Key Laboratory of Thermo-Fluid Science and Engineering, MOE, Xi'an Jiaotong University, Xi'an, China
[b] School of Mechanical and Aerospace Engineering, Nanyang Technological University, Singapore

ARTICLE INFO

Keywords:
Pore scale
Phase change material
Interfacial thermal resistance
Lattice Boltzmann method
Conjugate heat transfer

ABSTRACT

The performance of phase change materials (PCM) in the latent heat thermal storage system can be improved by doping highly conductive additives to enhance the thermal conduction. In this work, a pore-scale enthalpy-based lattice Boltzmann model is developed to investigate the melting performance of the PCM doped with porous media. The general conjugate boundaries between the doped additives and PCM are properly handled to ensure the continuity of heat flux even when interfacial thermal resistance or local thermal non-equilibrium state cannot be neglected. After code validations, the effects of doping additives on the melting rate of PCM are systematically investigated. The results show that although doping high thermal conductivity additives can enhance the heat conduction, it also significantly reduces the intensity of natural convection. Whether doping additives enhance the melting rate of PCM or not depends on the Rayleigh number and doping content. The melting rate of PCM can be optimized by a proper configuration of doping particles, with a high (low) doping content at the bottom (upper) parts of domain. Furthermore, the interfacial thermal resistance can significantly reduce the melting rate when the ratio of interfacial thermal resistance to bulk conductance resistance is larger than 0.01.

1. Introduction

The development of renewable energy, such as the solar energy, is of great significance due to the increasing severe energy crisis and environmental issues. In solar thermal systems, the energy storage technologies play a critical role in addressing the intermittent and unstable issues of solar energy. Among them, latent heat thermal energy storage (LHTES) is one of the most efficient techniques to store thermal energy because it has a large heat storage capacity and can be operated at a nearly constant working temperature [1,2].

The thermal performance of the LHTES depends on the thermal properties of the phase change material (PCM). Unfortunately, the thermal conductivity of most PCMs is rather low, which limits the energy storage efficiency. To improve the performance of the LHTES, much efforts have been made in the past decades. Generally, enhancing the effective thermal conductivity of PCMs is always a direct and efficient approach to improve melting rates by doping high thermal conductivity materials, such as the nanoparticles, metal foams, expanded graphite, and so on [3–5].

Due to the existence of heat-conduction enhanced particles or metal foams, the behaviors of heat transfer and natural convection inside the PCMs are greatly affected when the solid-liquid phase change process occurs. To obtain the understandings of how the additives affects the thermal performance of the PCM, many experimental [6–8] and numerical studies [9–11] have been conducted in the past decades. For the existing numerical models, there exist two kinds of approaches at different scales: representative elementary volume (REV) models and the pore-scale models. In the REV model, several empirical correlations should be employed to determine the macroscopic quantities (such as permeability, effective thermal conductivity) of the entire domain to close the models. Thus, the accuracy of the REV model depends on the choice of empirical correlations, and it cannot capture the detailed local information of dynamic flow and heat transfer inside pores [4,12–14]. In contrast, the pore-scale model can take the realistic porous structure as a geometry input, which enables it to consider the effect of realistic porous structure (or particle configuration) and provides a great promise in illuminating the underlying physical insights of phase change occurring within the complex porous microstructure.

Several studies have been performed to investigate the solid-liquid phase change process of the PCMs at the pore scale. Chen et al. [15] carried out a pore-scale study on the melting performance of PCMs embedded in metal foams and showed a significant enhancement effect

* Corresponding author at: Key Laboratory of Thermo-Fluid Science and Engineering, MOE, Xi'an Jiaotong University, Xi'an, China.
E-mail address: fangwenzhen76@gmail.com (W.-Z. Fang).

https://doi.org/10.1016/j.icheatmasstransfer.2020.104631

Available online 19 May 2020

on the melting. Feng et al. [16] compared the pore-scale and REV-scale simulation results of melting phase change process in a finned metal foam, and demonstrated that they are in good agreement. Ren et al. [17] performed a comparative pore-scale study to illustrate the effectiveness of improving the melting performance of PCMs doped with nanoparticles and metal foams. Li et al. [18] investigated the gravity effects on the pore-scale phase change process of PCMs filled with the metal foam. In the previous pore-scale models, no interfacial thermal resistance between the additives and PCMs is considered and heat transfer is assumed at the thermal equilibrium state, which corresponds to the one-temperature model (local thermal equilibrium) in the macroscopic model [13]. If the interfacial thermal resistance between the additives and PCMs is non-negligible or the local thermal equilibrium is not assured at the interface due to the markedly different diffusivity of additives and PCMs, a proper additional boundary treatment should be applied for the pore-scale model, which is corresponding to the two-temperature model (local thermal non-equilibrium) in the macroscopic model [4,19]. However, to the best of our knowledge, there are no pore-scale studies which can consider effects of the interfacial thermal resistance between the additives and PCMs or local thermal non-equilibrium situation. In this work, we aim to develop a pore-scale model which can handle such issues.

The lattice Boltzmann method (LBM) has been developed as an efficient numerical method to simulate complex fluid dynamics and heat transfer problems, including multiphase flow, reactive transports, phase change problems and fluid-structure interactions, and so on [20–22]. Recently, the LBM has also been developed to solve the solid-liquid phase change problems. The approaches to solve the solid-liquid phase change problems can be divided into two categories: phase-filed method [23] and enthalpy-based method [24–26]. In the enthalpy-based method, the liquid fraction of the PCM at each node is determined by the local value of enthalpy, which is used to capture the solid-liquid interfaces. The enthalpy-based LB model was first proposed by Jiang et al. [25] to solve the conduction-dominated solid-liquid phase change problem, in which an iterative solution is adopted to deal with the non-linear source term. Subsequently, Huber et al. [27] extended Jiang's model to be applicable for the solid-liquid phase change problem induced by the natural convection. To avoid the iterative solutions in solving the non-linear source term in the energy governing equation, Eshraghi and Felicelli [28] proposed an implicit scheme while Huang et al. [29] developed a thermal LB model based on a new equilibrium temperature distribution function. The LBM is particularly successful in handling complex boundary conditions owing to its kinetic nature. In the pore-scale LB modeling, the interaction at the fluid-solid interface can be easily dealt with by the bounce-back scheme. However, heat transfer through heterogeneous porous media should be considered as a conjugate heat transfer process, in which a proper treatment at the fluid-solid interface should be implemented to ensure the continuity of heat flux. The pioneer work to deal with the conjugate heat or mass transfer in LB models were limited to the steady state [30]. Due to the efforts of many researchers, several LB models were developed to be suitable for the transient situations [31–34].

In this paper, a pore-scale LB model is developed to investigate the transient solid-liquid phase change process of the PCM doped with the heat-conduction enhanced additives, which overcomes the previous pore-scale LB models that cannot consider effects of interfacial thermal resistance between the particle and PCM or local thermal non-equilibrium situation. The present pore-scale model can describe the interactions between the particles and PCM and elaborate how the particle configurations affect the melting performance of PCMs. In addition, an optimal particle configuration is proposed to enhance the melting rate. In this work, effects of the Rayleigh number, particle doping content, particle configurations, thermal conductivity of the particles, and interfacial thermal resistance on the melting performance of the PCM are systematically investigated.

2. Numerical simulation

2.1. LBM for fluid flow

In this study, a D2Q9 single-relation-time LB model is adopted to solve the natural convection induced by temperature gradient. The evolution equation of the density distribution function considering the buoyancy force can be expressed as follows [35,36]:

$$f_i(\boldsymbol{x}+\boldsymbol{c}_i\Delta t, t+\Delta t) - f_i(\boldsymbol{x},t) = -\frac{1}{\tau_f}[f_i(\boldsymbol{x},t) - f_i^{\mathrm{eq}}(\boldsymbol{x},t)] + \Delta t F_i \tag{1}$$

where f_i is the distribution function along the i direction at the lattice site $\boldsymbol{x}$ and time t;f^{eq} is the equilibrium distribution function

$$f_i^{\mathrm{eq}} = \omega_i\rho\left[1 + \frac{3}{c^2}(\boldsymbol{c}_i\cdot\boldsymbol{u}) + \frac{9}{2c^4}(\boldsymbol{c}_i\cdot\boldsymbol{u})^2 - \frac{3}{2c^2}u^2\right] \tag{2}$$

whereω_i is the weight parameter, and $\omega_0 = 4/9$,$\omega_{1\sim4} = 1/9$, $\omega_{5\sim8} = 1/36$ for D2Q9 model; and $\boldsymbol{c}_i$ is the discrete velocity, which is defined as:

$$\boldsymbol{c}_i = \begin{cases} (0,0)c & i = 0 \\ (\pm 1,0)c,\ (0,\pm1)c, & i = 1,\ldots,4 \\ (\pm 1,\pm1)c & i = 5,\ldots,8 \end{cases} \tag{3}$$

where $c = \Delta x/\Delta t$, where$\Delta x$is the space step and Δt is the time step.

The body force term $F_i$in Eq. (1) is developed by Guo et al. [37]:

$$F_{\mathrm{i}} = \omega_{\mathrm{i}}\left(1 - \frac{1}{2\tau_f}\right)\left(\frac{\boldsymbol{c}_{\mathrm{i}} - \mathbf{u}}{c_{\mathrm{s}}^2} + \frac{\boldsymbol{c}_{\mathrm{i}}\cdot\mathbf{u}}{c_{\mathrm{s}}^4}\boldsymbol{c}_{\mathrm{i}}\right)\cdot\mathbf{f} \tag{4}$$

where $\boldsymbol{f}$ is the buoyancy force, and can be calculated based on Boussinesq assumption:

$$\mathbf{f} = \rho\mathbf{g}\beta(T - T_{\mathrm{ref}}) \tag{5}$$

where $\boldsymbol{g}$ is the gravity acceleration; β is the expansion coefficient of fluids; and T_{ref} is the reference temperature.

The relation between the relaxation time coefficient (τ_f) and kinematic viscosity (ν) yields

$$\nu = \frac{1}{3}(\tau_f - 0.5)\frac{\Delta x^2}{\Delta t} \tag{6}$$

The macroscopic density and velocity can be obtained by

$$\rho = \sum_i f_i \tag{7}$$

$$\rho\boldsymbol{u} = \sum_i f_i\mathbf{e}_i + \frac{\Delta t}{2}\mathbf{f} \tag{8}$$

2.2. LBM for heat transfer

For the heat transfer in the fluid and solid domains, the evolution equation of temperature distribution function can be expressed as

$$g_i(\boldsymbol{x}+\boldsymbol{c}_i\Delta t, t+\Delta t) - g_i(\boldsymbol{x},t) = -\frac{1}{\tau_{\mathrm{T}}}[g_i(\boldsymbol{x},t) - g_i^{\mathrm{eq}}(\boldsymbol{x},t)] + \Delta t\omega_i S \tag{9}$$

where g_i is the temperature distribution function, and g_i^{eq} is the corresponding equilibrium temperature distribution

$$g_i^{\mathrm{eq}} = T\left(\omega_i + \frac{1}{2}\boldsymbol{c}_i\cdot\mathbf{u}\right) \tag{10}$$

where ω_i is the weight parameter, defined as

$$\omega_i = \begin{cases} \omega_0 & i = 0 \\ (1-\omega_0)/4 & i = 1,\ 2,\ 3,\ 4 \end{cases} \tag{11}$$

In this work, $\omega_0 = 1/3$. The relation between the temperature relaxation time coefficient and thermal diffusivity is

$$a = \frac{1}{2}(1-\omega_0)\left(\tau_T - \frac{1}{2}\right)\frac{\Delta x^2}{\Delta t} \tag{12}$$

The local temperature can be calculated by

$$T = \sum_i g_i \tag{13}$$

2.3. LBM for solid-liquid phase change problem

For heat transfer equation concerning solid-liquid phase change problem, the source term in Eq. (9) is

$$S = -\frac{\partial \varphi_l}{\partial t}\frac{L_f}{c_p} \tag{14}$$

where φ_l is the volume fraction of liquid phase; and L_f is the latent heat of phase change materials. In this study, an explicit iterative solution is adopted to deal with the nonlinear source term [25,27].

$$\begin{aligned} g_i^k(\boldsymbol{x}+\boldsymbol{e}_i\Delta t, t+\Delta t) &= g_i(\boldsymbol{x},t) - \frac{1}{\tau_T}[g_i(\boldsymbol{x},t) - g_i^{eq}(\boldsymbol{x},t)] + \Delta t\omega_i\frac{L_f}{c_p} \\ &\quad [\varphi_l^{k-1}(\boldsymbol{x},t+\Delta t) - \varphi_l(\boldsymbol{x},t)] \end{aligned} \tag{15}$$

where the superscript k represents the kth iteration at each time step.

An enthalpy-based method is adopted to track the solid-liquid phase change interface in this study. The local enthalpy can be determined by the local temperature and liquid fraction

$$En^k = c_p T^k + L_f \varphi_l^{k-1} \tag{16}$$

where En^k and T^k are the enthalpy and temperature, respectively. The volume fraction of the liquid can be updated by

$$\varphi_l^k = \begin{cases} 0 & En^k < En_s = c_p T_m \\ \dfrac{En^k - En_s}{En_l - En_s} & En_s \le En^k \le En_l = En_s + L_f \\ 1 & En^k > En_l = En_s + L_f \end{cases} \tag{17}$$

where En_s and En_l are enthalpies of the solid and liquid state of the phase change material at the melting temperature, respectively; and T_m is the melting temperature.

2.4. Treatment of conjugate conditions

Through the Chapman-Enskog expansion, the temperature evolution equation of Eq. (9) is retrieved to the following macroscopic governing eq. [32]

$$\frac{\partial T}{\partial t} + \nabla\cdot(\mathbf{u}T) = \nabla\cdot(a\nabla T) + S \tag{18}$$

Thus, the conservative flux at the interface is $a\nabla T$ rather than heat flux $\lambda\nabla T$. If the volumetric specific heat ρc_p is varying in the computational domain, an additional treatment should be applied to deal such conjugate boundary conditions.

Considering a conjugate heat transfer process in a heterogeneous medium, the general boundary conditions at the conjugate interfaces can be expressed as [34,38]:

$$\alpha_{11}^{A}T^{A} + \alpha_{12}^{A}\frac{\partial T^{A}}{\partial \boldsymbol{n}^{A}} = \alpha_{11}^{B}T^{B} + \alpha_{12}^{B}\frac{\partial T^{B}}{\partial \boldsymbol{n}^{B}} + c_1 \tag{19.a}$$

$$\alpha_{21}^{A}T^{A} + \alpha_{22}^{A}\frac{\partial T^{A}}{\partial \boldsymbol{n}^{A}} = \alpha_{21}^{B}T^{B} + \alpha_{22}^{B}\frac{\partial T^{B}}{\partial \boldsymbol{n}^{B}} + c_2 \tag{19.b}$$

where subscripts A and B represent component A and component B, respectively. If coefficients in Eq. (19) are specified, then one can recover a specific interfacial boundary condition. Particularly, with $\alpha_{11}{}^{A} = \alpha_{11}{}^{B} = 1$, $\alpha_{12}{}^{A} = \alpha_{12}{}^{B} = 0$, $c_1 = 0$ and $\alpha_{21}{}^{A} = \alpha_{21}{}^{B} = 0$, $\alpha_{22}{}^{A} = -\lambda^{A}$, $\alpha_{22}{}^{B} = \lambda^{B}$, $c_2 = 0$, one has

$$T^{A} = T^{B} \tag{20.a}$$

$$-\lambda^{A}\frac{\partial T^{A}}{\partial \boldsymbol{n}^{A}} = \lambda^{B}\frac{\partial T^{B}}{\partial \boldsymbol{n}^{B}} \tag{20.b}$$

which can ensure continuities of temperature and heat flux at interfaces.

If the interfacial thermal resistance cannot be neglected, the following boundary conditions should be applied

$$T^{A} - T^{B} = R_i\lambda^{A}\frac{\partial T^{A}}{\partial \boldsymbol{n}^{A}} \tag{21.a}$$

$$-\lambda^{A}\frac{\partial T^{A}}{\partial \boldsymbol{n}^{A}} = \lambda^{B}\frac{\partial T^{B}}{\partial \boldsymbol{n}^{B}} \tag{22.b}$$

where R_i denotes interfacial thermal resistance.

The conjugate boundary conditions of Eq. (19.a) and Eq. (19.b) can be decomposed into two Robin boundaries, respectively. Thus, we first introduce the treatment of Robin equation in LB community. The general Robin boundary condition can be expressed as

$$\alpha_1 T + \alpha_2\frac{\partial T}{\partial \boldsymbol{n}} = \alpha_3 \tag{23}$$

If the interface is put at the middle of two nodes, the unknown temperature distribution functions at the interfaces can be determined by [34,38]:

$$g_i(\boldsymbol{x}, t+\Delta t) = \frac{-p\Delta x + q}{p\Delta x + q}\overline{\overline{g}}_{\bar{i}}(\boldsymbol{x},t) + \frac{2\omega_i\alpha_3\Delta x}{p\Delta x + q} \tag{24}$$

where $\overline{\overline{g}}$ represents the post-collision distribution function; the subscript $\bar{i}$ denotes the direction opposite to i direction; p and q have the following expression:

$$p = \alpha_1 - \frac{(\boldsymbol{u}\cdot\boldsymbol{c}_i)}{a}\alpha_2,\ q = \frac{\alpha_2\Delta x^2}{3a\Delta t} \tag{25}$$

With the help of Eq. (24), one can derive the unknown temperature distribution functions for the conjugate heat transfer conditions expressed in Eq. (19.a) and Eq. (19.b):

$$g_i(\boldsymbol{x}^{A}, t+\Delta t) = \frac{1}{c_{22}^{A}c_{12}^{B} - c_{12}^{A}c_{22}^{B}}(c_{22}^{A}\varphi_1 - c_{12}^{A}\varphi_2) \tag{26.a}$$

$$g_{\bar{i}}(\boldsymbol{x}^{B}, t+\Delta t) = \frac{1}{c_{22}^{A}c_{12}^{B} - c_{12}^{A}c_{22}^{B}}(c_{22}^{A}\varphi_1 - c_{12}^{A}\varphi_2) \tag{26.b}$$

with

$$\varphi_1 = c_{12}^{B}c_{11}^{A}\overline{\overline{g}}_{\bar{i}}(\boldsymbol{x}^{A},t) - c_{12}^{A}[c_{11}^{B}\overline{\overline{g}}_{\bar{i}}(\boldsymbol{x}^{B},t) - c_{12}^{B}c_1] \tag{27.a}$$

$$\varphi_2 = c_{22}^{B}c_{21}^{A}\overline{\overline{g}}_{\bar{i}}(\boldsymbol{x}^{A},t) - c_{22}^{A}[c_{21}^{B}\overline{\overline{g}}_{\bar{i}}(\boldsymbol{x}^{B},t) - c_{22}^{B}c_2] \tag{27.b}$$

and

$$c_{11}^{A} = c_{11}^{B} = \frac{-p\Delta x + q}{p\Delta x + q},\quad c_{12}^{A} = c_{12}^{B} = \frac{2\omega_i\Delta x}{p\Delta x + q} \tag{28.a}$$

$$c_{21}^{A} = c_{21}^{B} = \frac{-p\Delta x + q}{p\Delta x + q},\quad c_{22}^{A} = c_{22}^{B} = \frac{2\omega_i\Delta x}{p\Delta x + q} \tag{28.b}$$

2.5. Computational domain and boundary condition

The PCMs are filled with porous media, such as the metal foams and heat-conduction enhanced particles, to enhance their effective thermal conductivity. Since our simulations are on the basis of two-dimensional results, the network of the metal foam cannot be fully resolved. Thus, the porous media is assumed to be composed of randomly dispersive particles and pores, as shown in Fig. 1. The effective particle diameter is set to be 0.6 mm, which mimics the effective diameter of skeleton of metal foam or submillimeter doping particles. In simulations, the

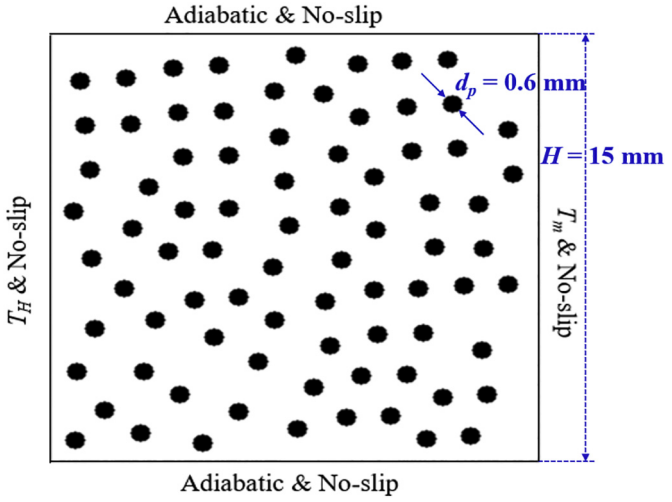

Fig. 1. Computational domain and boundary conditions (porosity: 0.9).

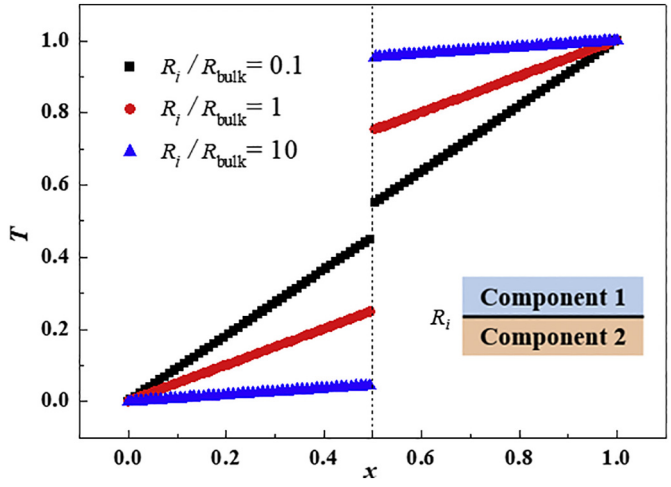

Fig. 2. Conduction in a dual-component medium with the interfacial thermal contact resistance.

computational domain is 15 mm × 15 mm discretized by a 300 × 300 grid system. Initially, the PCM is assumed to be solid state and at the melting temperature T_m. A higher temperature is applied at the left side to heat the entire system and the right side is maintained to the melting temperature, while the top and bottom boundaries are set to be adiabatic. All these four boundaries are set to be the no-slip condition for the flow boundaries. As for the solid-liquid interfaces, no-slip conditions are assigned for the flow boundaries while conjugate boundaries are applied for the heat transfer boundaries. The detailed treatments of conjugate boundaries are introduced in Section 2.4. Although this work is limited to the two-dimensional domain doped with dispersed particles, its applications in three-dimensional cases or PCM filled in porous metal foams are straightforward.

2.6. Thermal physical property

In this work, the studied PCM is a binary molten salt Li_2CO_3-K_2CO_3 with a mole ratio 62:38, and its thermal physical properties are list in Table 1. To improve the heat transfer performance, high thermal conductivity additives (such as copper) are doped into the PCMs. The density of the cooper is 8954 kg/m^3; the specific capacity is 383 J/(kg·K) and thermal conductivity is 400 W/(m·K). To investigate effects of thermal conductivity of doped additives on the thermal performance of the PCM, the thermal conductivities of the particles are varied from 0.6 W/(m·K) to 400 W/(m·K) in this study.

3. Validations

3.1. Conjugate boundary condition

Consider a one-dimensional heat transfer process in a dual-component medium. The numerical results of the heat transfer process in a dual-component medium with the interfacial thermal contact resistance are shown in Fig. 2. In this case, thermal conductivities are all 1 W/(m·K) and layer thicknesses are all 0.5 m for two components, resulting in a total bulk thermal resistance of 1 m^2·K/W. At the steady state, the theoretical result of temperature drop at the interface can be obtained by

$$\frac{\Delta T}{(T_{up} - T_{down})} = \frac{R_i}{R_i + R_{bulk}} \tag{29}$$

The above conjugate boundary is implemented with the method introduced in Section 2.4. The numerical results of temperature drop at the interface of $R_i / R_{bulk} = 0.1$, $R_i / R_{bulk} = 1$ and $R_i / R_{bulk} = 10$ are 0.0909, 0.5 and 0.909, respectively, which are identical to the theoretical results.

Table 1
The thermal properties of the PCM [17].

Physical property	Li_2CO_3 -K_2CO_3, mole ratio:62:38
Density ρ (kg·m^{-3})	1990
Specific capacity C_p (J·kg^{-1}·K^{-1})	1600
Thermal conductivity λ_f (W·m^{-1}·K^{-1})	0.6
Latent heat L_f (kJ·kg^{-1})	342
Melting temperature T_m (K)	759
Viscosity μ (kg·m^{-1}·s^{-1})	0.0055

3.2. LBM for solid-liquid phase change

In this section, the conduction melting process of the PCM in a semi-infinite domain is considered. Initially, the PCM is at the solid state and melting temperature $T_m = 0$. Then, the left boundary is subjected to a higher temperature $T_h = 1$. The temperature response in the fluid domain can be calculated by [27]:

$$T(x,t) = T_h - (T_h - T_m)\frac{\mathrm{erf}(x/2\sqrt{at})}{\mathrm{erf}(\gamma)}, \quad 0 \le x \le x_m \tag{30}$$

where a is the thermal diffusivity; x_m is the position of melting front (solid-liquid interface), which is determined by

$$x_m(t) = 2\gamma\sqrt{at} \tag{31}$$

where γ is the solution to the transcendental equation

$$\gamma \exp(\gamma^2)\,\mathrm{erf}(\gamma) = \frac{St}{\sqrt{\pi}} \tag{32}$$

where

$$St = \frac{c_p(T_h - T_m)}{L_f} \tag{33}$$

The numerical results of the position of melting front and the temperature field obtained by the present method are shown in Fig. 3, which agree well with theoretical results.

4. Results and discussion

4.1. Solid-liquid phase change in a square cavity without particles

In this section, the melting rate of the PCM in a square cavity without any doped particles at different Rayleigh numbers are first

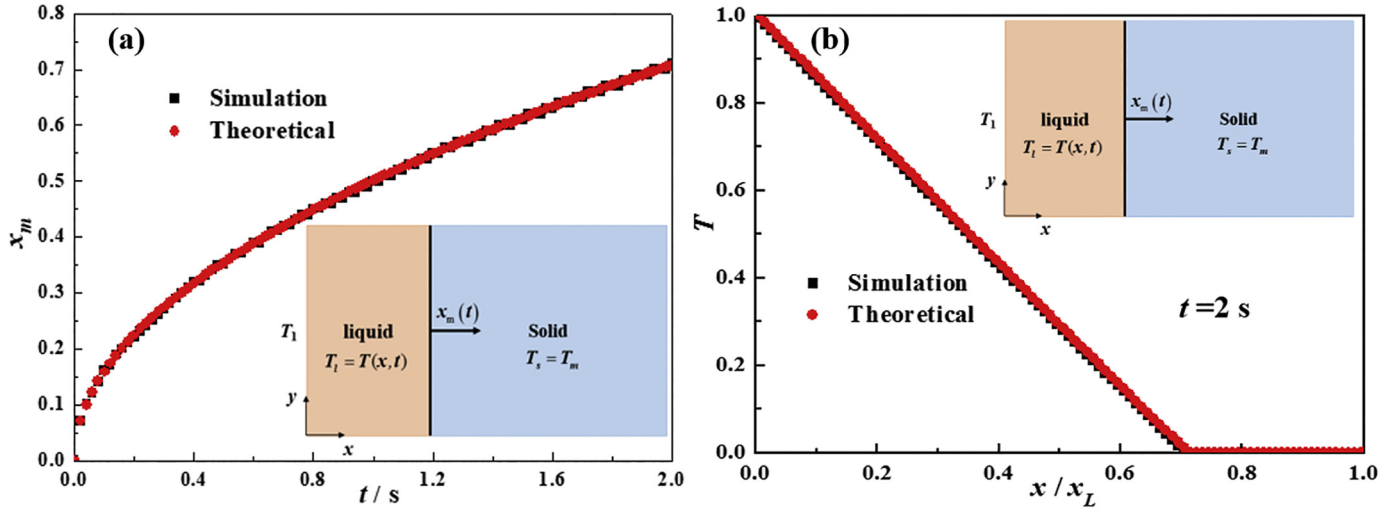

Fig. 3. Conduction melting in a semi-infinite domain (a) melting front position (b) temperature field.

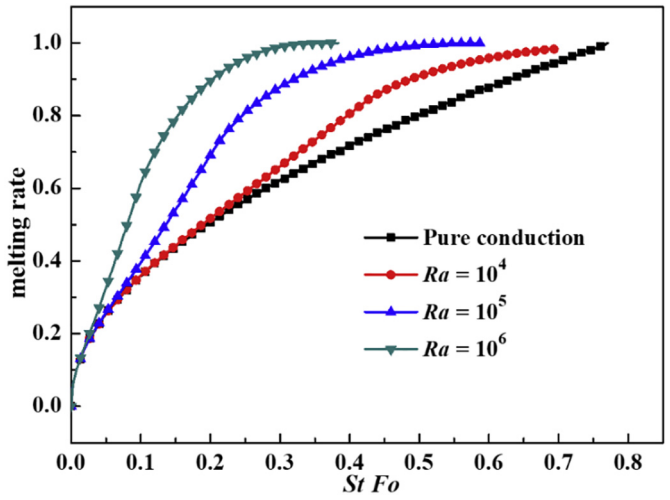

Fig. 4. The melting rates of PCMs at different Rayleigh number in a cavity without particles.

studied. The dependences of the melting rate on the dimensionless time $St \cdot Fo$ are shown in Fig. 4. The dimensionless numbers Ra, Fo are defined as follows:

$$Ra = \frac{g\beta\Delta TH^3}{a\nu} \tag{34}$$

$$Fo = \frac{at}{H^2} \tag{35}$$

where β is the expansion coefficient; a is the thermal diffusivity; H is the height of the square cavity. It can be seen that the melting rate of PCMs can be significantly enhanced due to the natural convection. Besides, the melting rate increases with the Ra number. At the beginning of the phase change process, the melting process is conduction-dominated, which results in a consistent melting rate among different Ra numbers. As the melting process continues, the fraction of liquid phase in the domain increases, and the effects of natural convection start to play an dominate role, which results in the deviations of the melting rate among different Ra numbers at later periods. At the time moment of $t = 10^6\ \Delta t$, comparisons of the solid-liquid interface and temperature distribution among different Ra numbers are shown in Fig. 5. It can be seen that due to the natural convection induced by the temperature difference, a clockwise vortex will appear in the fluid domain, which will significantly enhanced heat transfer rate and melting rate of the PCM. The melting rate of the PCM at the top side is superior to that at the bottom because the direction of the vortex is clockwise. Therefore, the PCM at the bottom right corner of the entire system is the last region to be melted, causing the melting rate of the PCM slow down when the melting fraction is approaching 1. Such phenomenon is more obvious at a large Ra number (see Fig. 4).

4.2. Effect of the doping particle contents

In this section, the effects of the particle doping contents on the melting rate of PCMs are investigated. The comparisons of melting rate of PCMs with and without particles are shown in Fig. 6. The doping volume fraction of the particle is 5% ($\phi = 5\%$). It can be seen that the doping particle can improve the heat conduction process due to its higher thermal conductivity, and therefore the melting rate of PCMs doped with particles is superior to that without particles when the melting process is induced by pure conduction. However, the melting rate of PCMs doped with particle is slower than that without particles when $Ra = 10^6$. At the time moment of $t = 10^6\ \Delta t$, the detailed melting information of the solid-liquid interface and temperature distribution at different Ra numbers are shown in Fig. 7. Compared with the melting information shown in Fig. 5, it can be seen that the doping particles can speed up the heat conduction while significantly suppress the natural convection. Therefore, in a conduction-dominated melting process, the doped particles will increase the melting rate, while may suppress the melting rate in a convection-dominated melting process. When $Ra = 10^6$, the melting process is convection-dominated, resulting in the melting rate of the PCM doped with particles smaller than that of the PCM without particles.

Fig. 8 shows the comparisons of melting rates of PCMs among different doping particle contents and Ra numbers. It can be seen that the melting rate of PCMs induced by the pure conduction increases when the doping particle contents increase. The deviations of melting rate of PCMs between pure conduction ($Ra = 0$), $Ra = 10^4$, $Ra = 10^5$ and $Ra = 10^6$ decrease when the doping particle content increases. This is because the natural convection is highly suppressed at a higher doping particle content. When the particle content is higher than 5%, the melting rate of PCMs at $Ra = 10^4$ almost have no difference with that at pure conduction, which imply that the melting process of $Ra = 10^4$ is conduction dominated when $\phi \geq 5\%$.

4.3. Effect of particle configurations

In this section, the effects of particle configurations on the melting rate are investigated. At the moment of $t = 10^6\Delta t$, the comparisons of

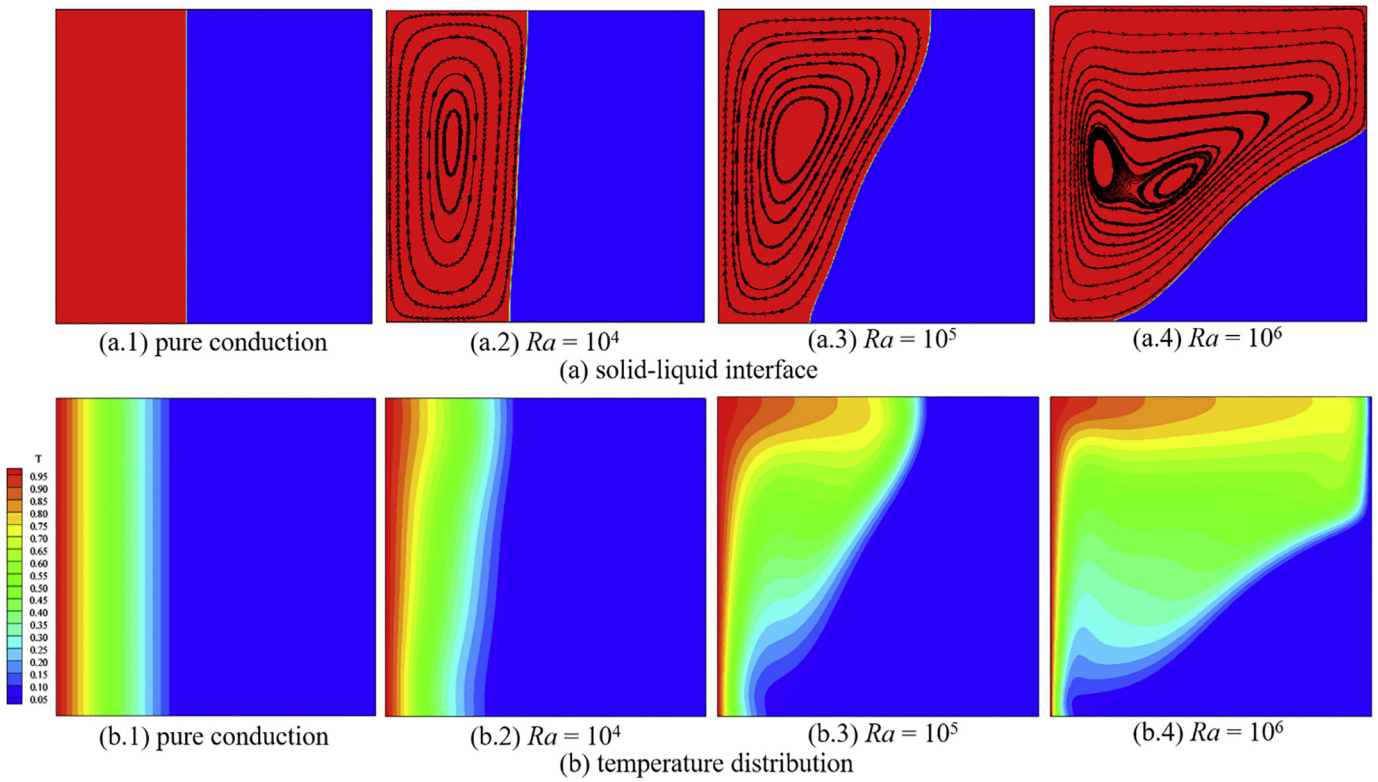

Fig. 5. Comparisons of solid-liquid interface and temperature distribution in a square cavity (without particles) among different *Ra* numbers (a) solid-liquid interface (b) temperature distribution.

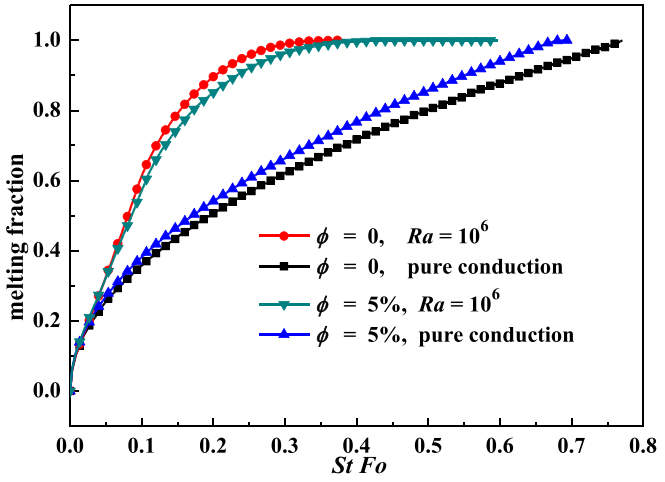

Fig. 6. Comparisons of melting rate of PCMs with and without particles (the doping particle content is $\phi = 5\%$).

solid-liquid interfaces and temperature field at different particle configurations are shown in Fig. 9. In this work, two kinds of particle configurations are designed and the particle doping contents are all 10%. The particles in pattern 1 are randomly distributed in the entire domain, while those in pattern 2 are hierarchical, with particle doping content equal to 0, 10%, 20% at the top, middle and bottom parts of domain, respectively. As discussed in Section 4.1, the vortex generated by the natural convection is clockwise, resulting in a negative flow velocity at the bottom of domain (opposite to the marching direction of solid-liquid interface). Therefore, the solid-liquid interface at the bottom part tends to recede back compared with the pure conduction situation. To reduce the absolute value of negative velocity and enhance the heat conduction at the bottom part, more particles are introduced at the bottom part while fewer particles are placed at the top part to enhance the natural convection. Fig. 10 shows the comparisons of the melting rate of PCMs among different particle configurations. It can be seen that the melting rate of PCMs induced by pure conduction between two configurations are almost identical since particle doping contents are the same. However, at $Ra = 10^5$, the melting rate of PCMs in the particle configuration with particle denser at the bottom and sparser at the top (pattern 2) is superior to that of the particle randomly distributed configuration (pattern 1). For the particle configuration in pattern 2, the natural convection is expected to be enhanced at the top part while the heat conduction is improved at the bottom part. Note that the waved temperature distribution as well as the solid-liquid interface are due to the existence of the heat-conduction enhanced particle.

4.4. Effects of the thermal conductivity of doping additives

Usually, porous media are imbedded into PCM to improve the thermal performance of PCM. Engineering materials including copper and aluminum oxide (Al_2O_3) are candidates as the porous media. In this section, effects of the thermal conductivity of doping additives on the melting rate of PCMs are investigated. The studied doping content is 10% and $Ra = 10^4$. The thermal conductivity of the PCM is 0.6 W/(m·K), while the thermal conductivity of doping additives ranges from 0.6 W/(m·K) (the same as the PCM), 27 W/(m·K) (Al_2O_3) [11] and 400 W/(m·K) (cooper). The effects of the thermal conductivity of doping additives on the melting rate of PCMs are shown in Fig. 11 (a). As expected, the melting rate of PCMs increases when the thermal conductivity of doping additives increases. In addition, the comparisons of temperature distributions along the central line of the domain are shown in Fig. 11 (b). It can be seen that the temperature drop across the highly conductive additives (cooper) is much smaller than that with thermal conductivity equal to PCM, which speeds up the melting process. However, when the ratio of λ_s / λ_p (where λ_s and λ_p are the

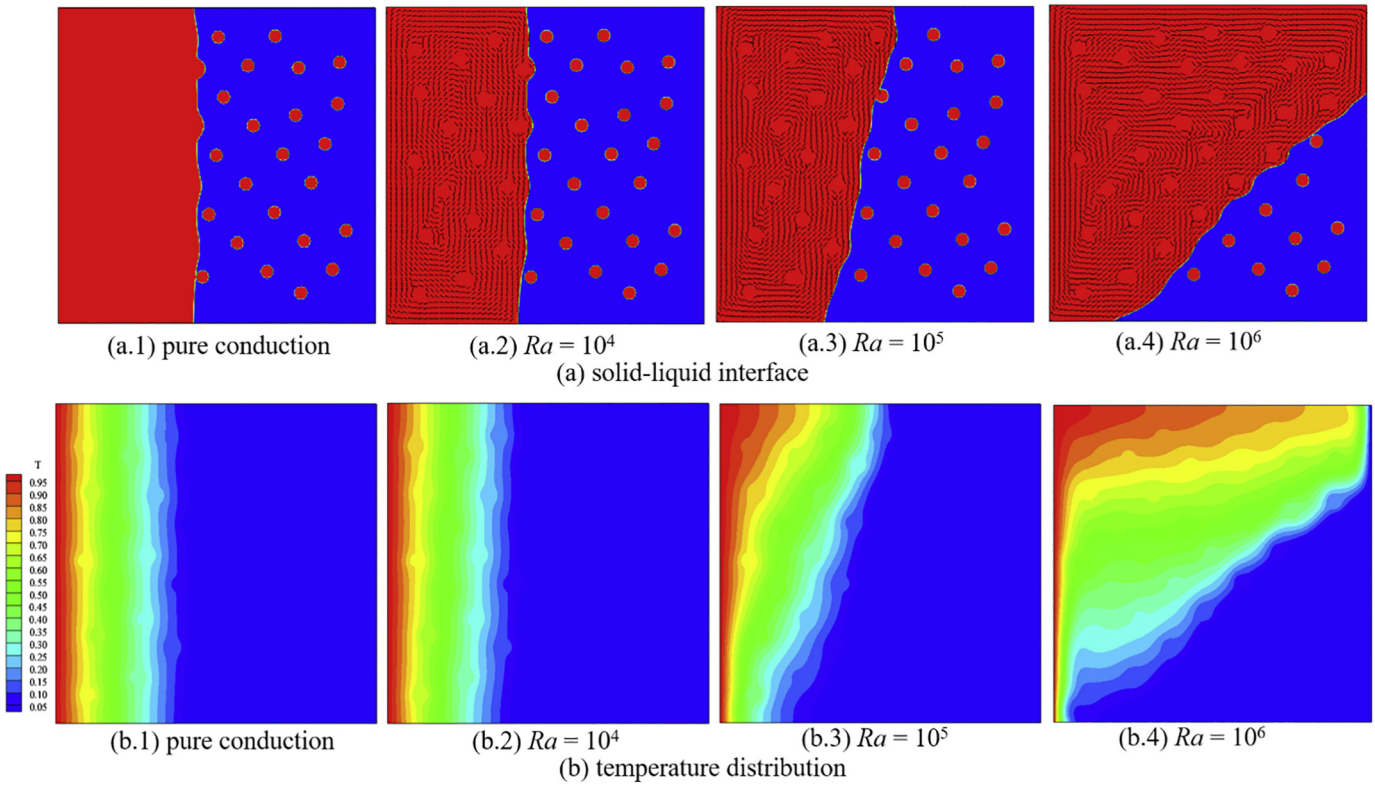

Fig. 7. Comparisons of detailed melting processes among different *Ra* numbers (ϕ = 5%) (a) solid-liquid interface (b) temperature distribution.

thermal conductivity of the additive and PCM, respectively) is over 45, it is not efficient to enhance the melting rate by further increasing the thermal conductivity of additives. It is because the heat-conduction enhanced particles are dispersed in the PCM and do not form a continuous heat conduction channel due to the low doping content. This is the reason why the metal foam is the favor one to enhance the melting rate. The effective thermal conductivity of the PCM doped with dispersive additives can be approximated determined by the Maxwell's law:

$$\frac{\lambda_e}{\lambda_p} = 1 + \frac{3(\alpha - 1)\phi}{(\alpha + 2) - (\alpha - 1)\phi} \tag{36}$$

where ϕ is the volume fraction of doping additives; $\alpha = \lambda_s / \lambda_p$ is the ratio of thermal conductivity between doping additives and the PCM. When the value of α goes to the infinity, λ_e/λ_p approaches a limit value $1 + 3\phi / (1\text{-}\phi)$.

4.5. Effects of interfacial thermal resistance

Due to the markedly different diffusivity of additives and PCMs, local thermal equilibrium is not assured at the interface. If the heat transfer is local thermal non-equilibrium or there exists interfacial thermal contact resistance between the PCM and doping additives, the temperature difference between the PCM and additives should be considered [39,40]. In this section, the effects of the interfacial thermal resistance on the melting rate of the PCMs are investigated. In nature, the value of interfacial thermal resistance depends on the contact materials, contact pressure and temperature. However, the most typical value of thermal contact resistance is in the order of 10^{-4} m^2·K/W [41], and thus the normalized interfacial thermal resistances R_i /R_{bulk} is in the order of 0.01, where $R_{bulk} = H / \lambda_p$ is the thermal conduction resistance when the entire system is filled with the PCM. Due to the lack of exact interfacial thermal resistance in literature, we varied interfacial thermal resistances R_i/R_{bulk} in this study, ranging from 0, 0.001, 0.01 to 0.1. The comparisons of the temperature distribution among different interfacial thermal resistance are shown in Fig. 12. The particle doping content is 10% and $Ra = 10^4$. Compared with the case without interfacial thermal resistance, the thermal propagation is slighted postponed for $R_i / R_{bulk} = 0.001$, while significant for the cases of $R_i / R_{bulk} = 0.01$ and $R_i / R_{bulk} = 0.1$. The comparisons of the melting rate

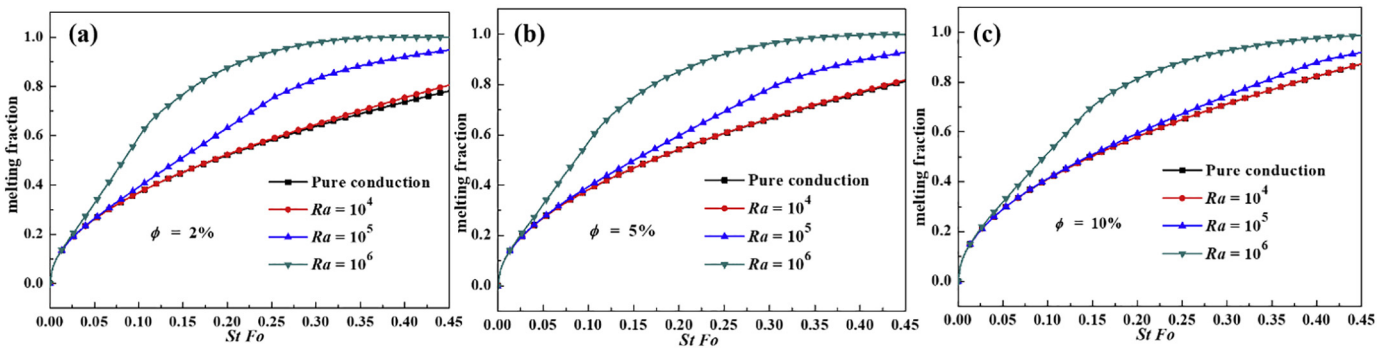

Fig. 8. Comparisons of melting rate among different doping contents (a) ϕ = 2% (b) ϕ = 5% (c) ϕ = 10%.

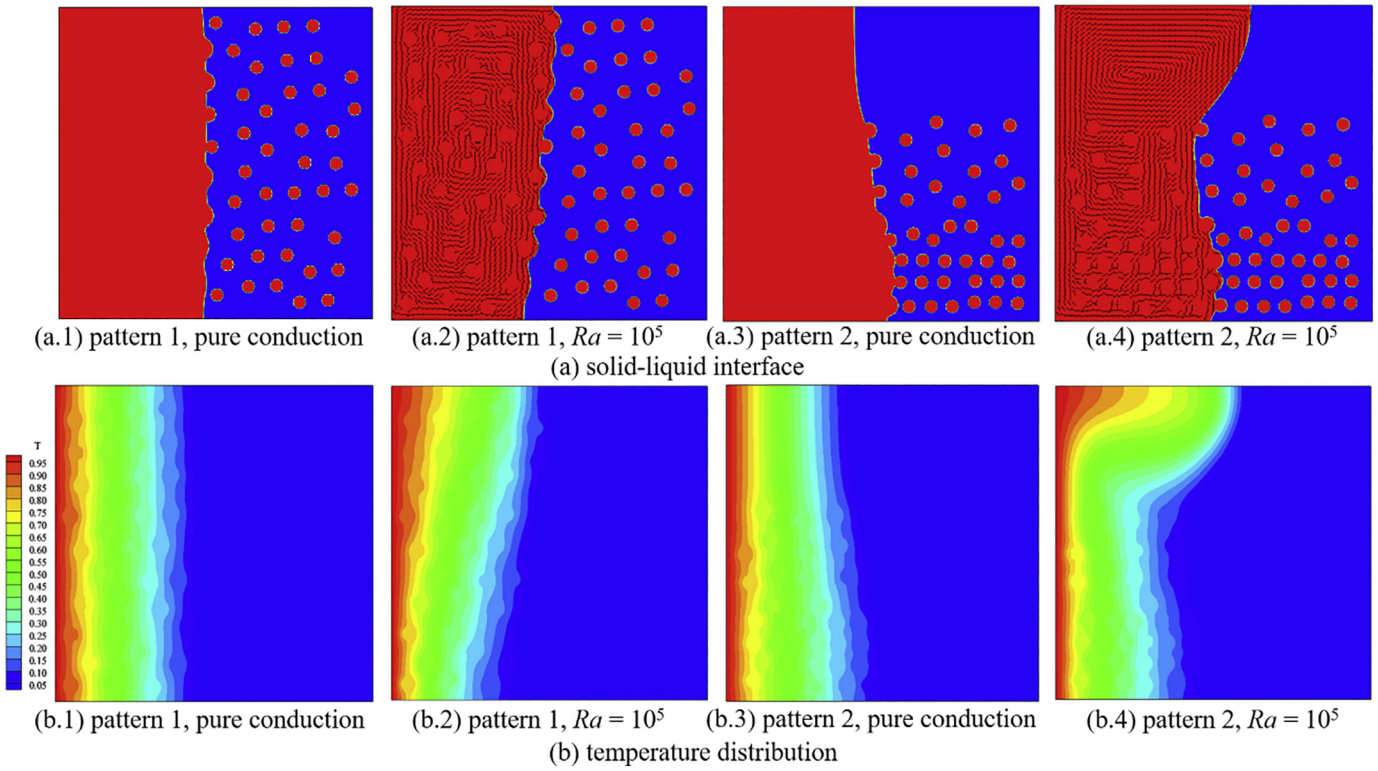

Fig. 9. Comparisons of melting information among different particle configurations (a) solid-liquid interface (b) temperature distribution (pattern 1: particle random distributed; pattern 2: dense particle at the bottom and sparse at the top).

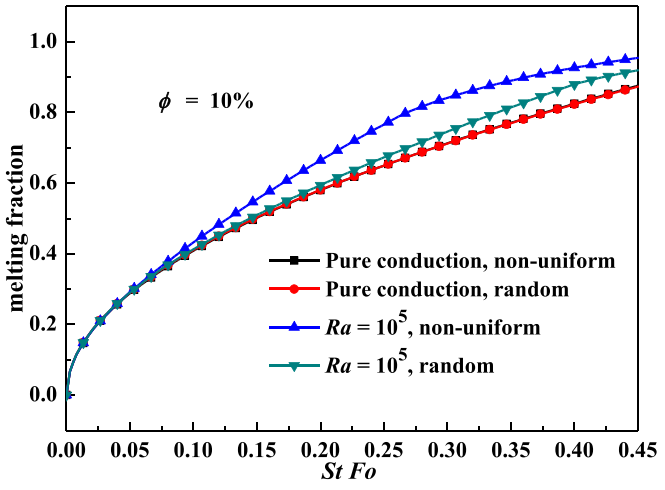

Fig. 10. Comparisons of melting rate of PCMs among different particle doping configuration (*random* represents particles are randomly distributed; *non-uniform* represents particles are in configuration with dense at the bottom and sparse at the top).

of PCMs and temperature distribution along the central line are shown in Fig. 13. It can be seen that the temperature drop at the interface increases with the value of R_i / R_{bulk}, which is significant for R_i / R_{bulk} = 0.1 while negligible for R_i / R_{bulk} = 0.001.

5. Conclusion

In this work, a pore-scale enthalpy-based lattice Boltzmann model is developed to investigate the solid-liquid phase change process of phase change materials doped with the conduction-enhanced particles. The interfacial conjugate heat transfer boundaries at the particle-fluid interfaces are properly dealt to ensure the continuity of the heat flux. The present model can consider the effects of interfacial thermal resistance between the doped particles and phase change materials or local thermal non-equilibrium condition on the melting process of the phase change materials. The effects of the doping content of particles, particle configuration, thermal conductivity of doping particles and interfacial thermal resistance on the melting rate of the phase change materials are systematically studied. The following conclusions can be drawn:

(1) The melting rate of the phase change materials significantly increases with the Rayleigh number if the entire domain is free of doping particles; the doping particles with the high thermal conductivity can enhance the heat conduction while significantly reduce the intensity of natural convection; Whether the doping particles enhance the melting rate of phase change materials or not depends on the Rayleigh number; With the increase of particle doping content, the natural convection is further suppressed, and when the volume fraction of doping particles is over 5%, the melting rate of $Ra = 10^4$ almost equals to that of the pure conduction;
(2) When the system is heated from the left side of the domain, the melting rate of the phase change material can be enhanced by increasing the particle doping content at the bottom part of domain and meanwhile reducing the particle doping content at the top part when the total doping content of practices are maintained;
(3) Increasing the thermal conductivity of doping particles can enhance the melting rate of the phase change materials, but the increase effect is no significant when the doping particles are dispersive in the domain. The melting rate of the phase change material increases with the decrease of interfacial thermal resistance. If R_i / $R_{bulk} \leq 0.001$, the interfacial thermal resistance almost has no influence on the melting rate, while it significantly reduces the melting rate and there are obvious temperature drops exist at the

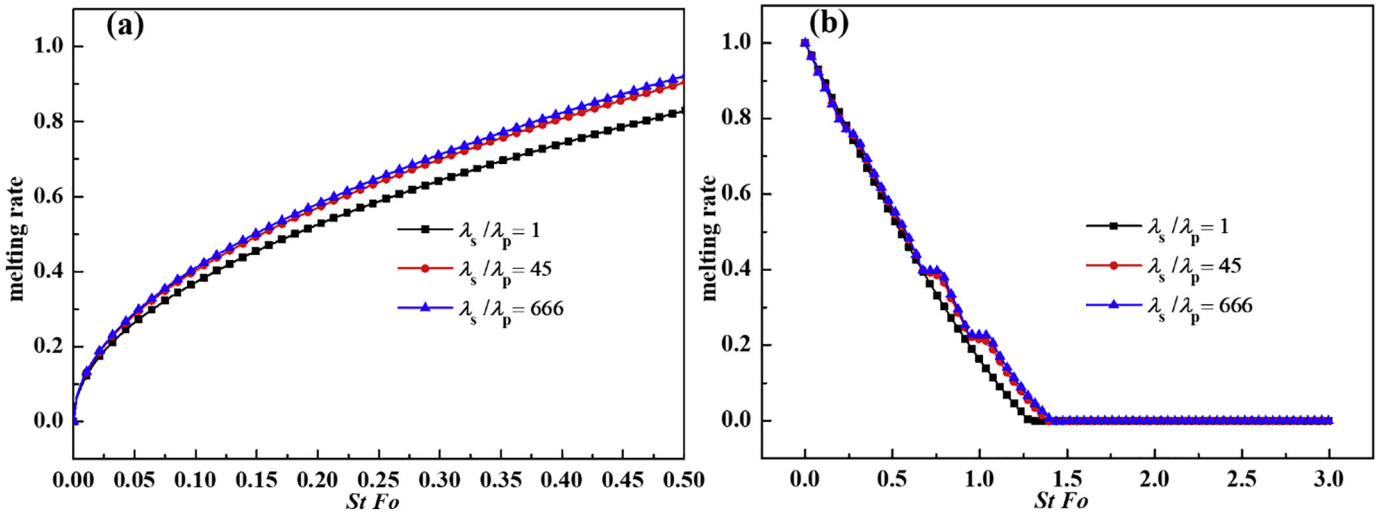

Fig. 11. Effects of the thermal conductivity of the doping additives on the melting rate of PCMs (a) melting rate (b) temperature distribution along the horizontal central line (λ_s and λ_p are the thermal conductivity of the additives and PCM, respectively).

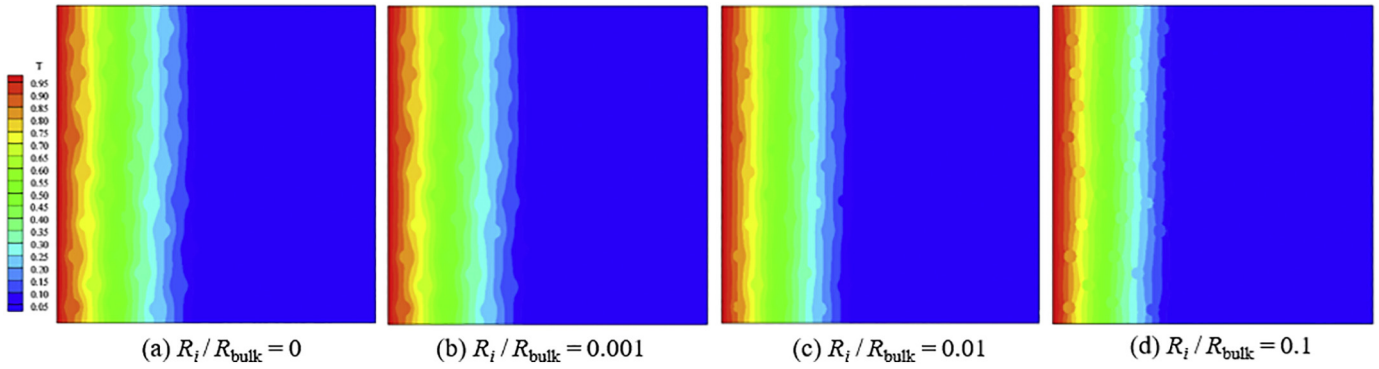

Fig. 12. Comparisons of temperature distributions among different interfacial thermal resistance.

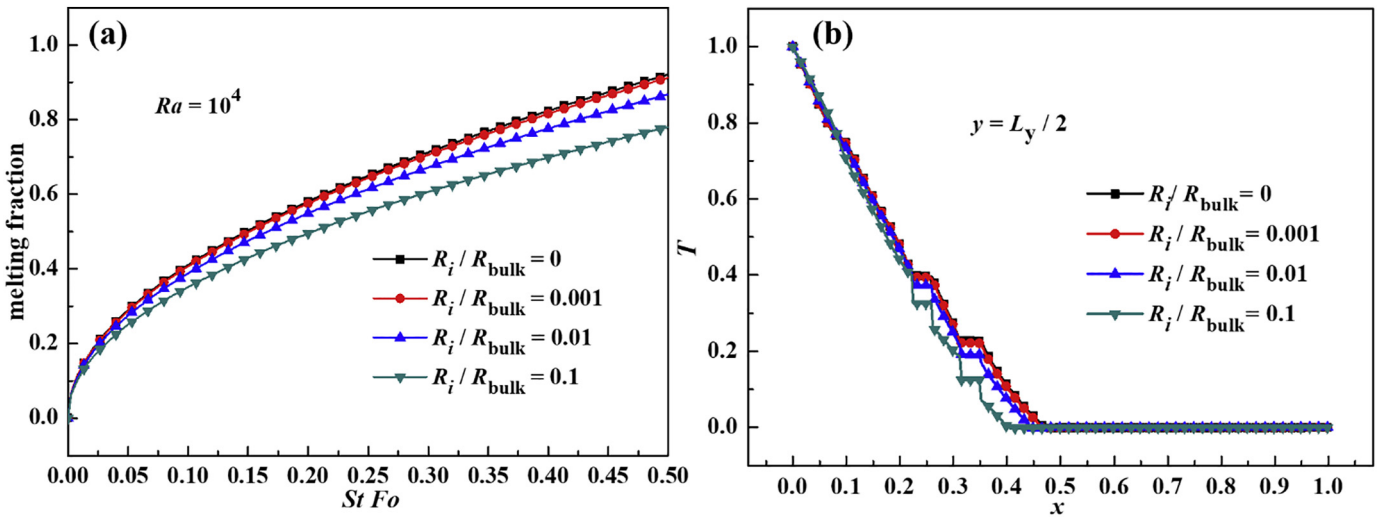

Fig. 13. Comparisons of the melting rate of PCMs among different interfacial thermal resistance (a) melting rate (b) temperature distribution along the central line.

interfaces when $R_i / R_{bulk} = 0.01$ and $R_i / R_{bulk} = 0.1$.

Credit author statement

W.Z.: Methodology, Code writing and Validation, Data analysis and Draft preparation.

Y.Q.: Methodology, Validation, Visualization and Writing-Reviewing and Editing.

C.Y.: Conceptualization and Writing-Reviewing and Editing.

W.Q.: Conceptualization and Writing-Reviewing and Editing.

Declaration of Competing Interest

The authors declare that they have no known competing financial interests or personal relationships that could have appeared to influence the work reported in this paper.

References

[1] F. Agyenim, N. Hewitt, P. Eames, M. Smyth, A review of materials, heat transfer and phase change problem formulation for latent heat thermal energy storage systems (LHTESS), Renew. Sust. Energ. Rev. 14 (2) (2010) 615–628.

[2] A. Sarı, A. Karaipekli, Thermal conductivity and latent heat thermal energy storage characteristics of paraffin/expanded graphite composite as phase change material, Appl. Therm. Eng. 27 (8–9) (2007) 1271–1277.

[3] Z. Huang, X. Gao, T. Xu, Y. Fang, Z. Zhang, Thermal property measurement and heat storage analysis of $LiNO_3$/KCl–expanded graphite composite phase change material, Appl. Energy 115 (2014) 265–271.

[4] Y. Tao, C. Lin, Y. He, Preparation and thermal properties characterization of carbonate salt/carbon nanomaterial composite phase change material, Energy Convers. Manag. 97 (2015) 103–110.

[5] L.C. Wei, J.A. Malen, Amplified charge and discharge rates in phase change materials for energy storage using spatially-enhanced thermal conductivity, Appl. Energy 181 (2016) 224–231.

[6] C. Zhao, W. Lu, Y. Tian, Heat transfer enhancement for thermal energy storage using metal foams embedded within phase change materials (PCMs), Sol. Energy 84 (8) (2010) 1402–1412.

[7] X. Xiao, P. Zhang, M. Li, Effective thermal conductivity of open-cell metal foams impregnated with pure paraffin for latent heat storage, Int. J. Therm. Sci. 81 (2014) 94–105.

[8] P. Zhang, X. Xiao, Z. Meng, M. Li, Heat transfer characteristics of a molten-salt thermal energy storage unit with and without heat transfer enhancement, Appl. Energy 137 (2015) 758–772.

[9] S. Krishnan, J.Y. Murthy, S.V. Garimella, A two-temperature model for solid-liquid phase change in metal foams, J. Heat Transf. 127 (9) (2005) 995–1004.

[10] Y. Feng, H. Li, L. Li, L. Bu, T. Wang, Numerical investigation on the melting of nanoparticle-enhanced phase change materials (NEPCM) in a bottom-heated rectangular cavity using lattice Boltzmann method, Int. J. Heat Mass Transf. 81 (2015) 415–425.

[11] Y. Xu, Q. Ren, Z.J. Zheng, Y.L. He, Evaluation and optimization of melting performance for a latent heat thermal energy storage unit partially filled with porous media, Appl. Energy 193 (2017) 84–95.

[12] Q. Liu, Y.L. He, Q. Li, Enthalpy-based multiple-relaxation-time lattice Boltzmann method for solid-liquid phase-change heat transfer in metal foams, Phys. Rev. E 96 (2) (2017) 023303.

[13] D. Gao, Z. Chen, Lattice Boltzmann simulation of natural convection dominated melting in a rectangular cavity filled with porous media, Int. J. Therm. Sci. 50 (4) (2011) 493–501.

[14] D. Gao, Z. Chen, L. Chen, A thermal lattice Boltzmann model for natural convection in porous media under local thermal non-equilibrium conditions, Int. J. Heat Mass Transf. 70 (2014) 979–989.

[15] Z. Chen, D. Gao, J. Shi, Experimental and numerical study on melting of phase change materials in metal foams at pore scale, Int. J. Heat Mass Transf. 72 (2014) 646–655.

[16] S. Feng, M. Shi, Y. Li, T.J. Lu, Pore-scale and volume-averaged numerical simulations of melting phase change heat transfer in finned metal foam, Int. J. Heat Mass Transf. 90 (2015) 838–847.

[17] Q. Ren, F. Meng, P. Guo, A comparative study of PCM melting process in a heat pipe-assisted LHTES unit enhanced with nanoparticles and metal foams by immersed boundary-lattice Boltzmann method at pore-scale, Int. J. Heat Mass Transf. 121 (2018) 1214–1228.

[18] X. Li, T. Ma, J. Liu, H. Zhang, Q. Wang, Pore-scale investigation of gravity effects on phase change heat transfer characteristics using lattice Boltzmann method, Appl. Energy 222 (2018) 92–103.

[19] W. Li, Z. Qu, Y. He, W. Tao, Experimental and numerical studies on melting phase change heat transfer in open-cell metallic foams filled with paraffin, Appl. Therm. Eng. 37 (2012) 1–9.

[20] W.Z. Fang, Y.Q. Tang, L. Chen, Q.J. Kang, W.Q. Tao, Influences of the perforation on effective transport properties of gas diffusion layers, Int. J. Heat Mass Transf. 126 (2018) 243–255.

[21] W.Z. Fang, Y.Q. Tang, C. Ban, Q.J. Kang, R. Qiao, W.Q. Tao, Atomic layer deposition in porous electrodes: a pore-scale modeling study, Chem. Eng. J. 378 (2019) 122099.

[22] W.Z. Fang, S. Ham, R. Qiao, W.Q. Tao, Magnetic actuation of surface walkers: the effects of confinement and inertia, Langmuir (2020), https://doi.org/10.1021/acs.langmuir.9b03487.

[23] I. Rasin, W. Miller, S. Succi, Phase-field lattice kinetic scheme for the numerical simulation of dendritic growth, Phys. Rev. E 72 (6) (2005) 066705.

[24] C. Zhang, H. Zhang, W.Z. Fang, Y.G. Zhao, C. Yang, Axisymmetric lattice Boltzmann model for simulating the freezing process of a sessile water droplet with volume change, Phys. Rev. E 101 (2) (2020) 023314.

[25] W.S. Jiaung, J.R. Ho, C.P. Kuo, Lattice Boltzmann method for the heat conduction problem with phase change, Numer. Heat Transf. B 39 (2) (2001) 167–187.

[26] W.Z. Fang, H. Zhang, C.Y. Zhang, C. Yang, Freezing process of ferrofluid droplets: numerical and scaling analyses, Physical Rev. Fluids 5 (2020) 053601.

[27] C. Huber, A. Parmigiani, B. Chopard, M. Manga, O. Bachmann, Lattice Boltzmann model for melting with natural convection, Int. J. Heat Fluid Flow 29 (5) (2008) 1469–1480.

[28] M. Eshraghi, S.D. Felicelli, An implicit lattice Boltzmann model for heat conduction with phase change, Int. J. Heat Mass Transf. 55 (9–10) (2012) 2420–2428.

[29] R. Huang, H. Wu, P. Cheng, A new lattice Boltzmann model for solid–liquid phase change, Int. J. Heat Mass Transf. 59 (2013) 295–301.

[30] J. Wang, M. Wang, Z. Li, A lattice Boltzmann algorithm for fluid–solid conjugate heat transfer, Int. J. Therm. Sci. 46 (3) (2007) 228–234.

[31] L. Li, C. Chen, R. Mei, J.F. Klausner, Conjugate heat and mass transfer in the lattice Boltzmann equation method, Phys. Rev. E 89 (4) (2014) 043308.

[32] H. Karani, C. Huber, Lattice Boltzmann formulation for conjugate heat transfer in heterogeneous media, Phys. Rev. E 91 (2) (2015) 023304.

[33] D. Gao, Z. Chen, L. Chen, D. Zhang, A modified lattice Boltzmann model for conjugate heat transfer in porous media, Int. J. Heat Mass Transf. 105 (2017) 673–683.

[34] Z. Hu, J. Huang, W.A. Yong, Lattice Boltzmann method for convection-diffusion equations with general interfacial conditions, Phys. Rev. E 93 (4) (2016) 043320.

[35] S. Chen, G.D. Doolen, Lattice Boltzmann method for fluid flows, Annu. Rev. Fluid Mech. 30 (1) (1998) 329–364.

[36] W.Z. Fang, L. Chen, Q.J. Kang, W.Q. Tao, Lattice Boltzmann modeling of pool boiling with large liquid-gas density ratio, Int. J. Therm. Sci. 114 (2017) 172–183.

[37] Z. Guo, C. Zheng, B. Shi, Discrete lattice effects on the forcing term in the lattice Boltzmann method, Phys. Rev. E 65 (4) (2002) 046308.

[38] J. Huang, W.A. Yong, Boundary conditions of the lattice Boltzmann method for convection–diffusion equations, J. Comput. Phys. 300 (2015) 70–91.

[39] W.Z. Fang, J.J. Gou, L. Chen, W.Q. Tao, A multi-block lattice Boltzmann method for the thermal contact resistance at the interface of two solids, Appl. Therm. Eng. 138 (2018) 122–132.

[40] Y.J. Dai, J.J. Gou, X.J. Ren, F. Bai, W.Z. Fang, W.Q. Tao, A test-validated prediction model of thermal contact resistance for ti-6Al-4V alloy, Appl. Energy 228 (2018) 1601–1617.

[41] M.M. Yovanovich, Four decades of research on thermal contact, gap, and joint resistance in microelectronics, IEEE Trans. Compon. Packag. Technol. 28 (2) (2005) 182–206.